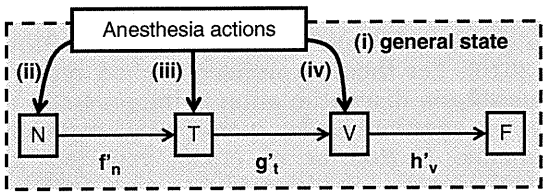

(i) Systemic physiology
- blood gas conditions
- cardiac output
- arterial blood pressure

(iii) Vasoactive signal Transmission
- release and uptake of transmitters
- efficiency of transmission
- turnover

(ii) Neural activity
- synaptic transmission
- pre-synaptic release
- post-synaptic receptors
- removal of transmitters
- membrane potentials

(iv) Vascular reactivity
- baseline CBF
- vascular tone
- vasomotion
- receptor functions
- calcium ion mobility

Figure 2 Summary of the effects of anesthesia on neurovascular coupling. The effects of anesthetics involve systemic physiology (i), neural processing (ii), vasoactive signal transmission (iii), and vascular responses (iv). Depending on the type and dose of anesthetic, the anesthesia differentially modifies the individual transfer functions of neural processing (f'_n), vasoactive signal transmission (g'_t), and vascular reactivity (h'_v). CBF, cerebral blood flow.

the temporal dynamics of vasodilation may vary between anesthetics. Finally, the quantitative coupling relationship of neurovascular responses is strongly influenced by anesthesia types and dosages. The fact that different anesthetics differentially modify the hemodynamic impulse response functions indicates that different anesthetics act specifically on the different cell populations that participate in the vasoactive pathways. In addition, this anesthesia interference may involve variations in baseline states, such as spontaneous neural activity, energy metabolism, and baseline CBF.

For *in-vivo* rodent somatosensory models, a large amount of neurovascular physiology and imaging data have been accumulated under α-chloralose anesthesia. Some findings might be specific to this anesthetic, such as the optimum stimulus frequency (Table 2) and low baseline CBF (Table 3). For repeated longitudinal experiments, isoflurane is recommended as an alternative agent because it provides easy control, good anesthesia recovery, and robust activity-induced vascular response that is comparable to that of α-chloralose in rat somatosensory models (Masamoto *et al*, 2007; Franceschini *et al*, 2010). Intravenous injection anesthesia (e.g., α-chloralose and medetomidine) carries concerns about the stability and reproducibility for long-term experiments (>3 hours), whereas urethane provides relatively long-term stability and balanced actions on multiple neurotransmitter receptors. Although some anesthetics, such as isoflurane, pentobarbital, and medetomidine, directly affect vascular physiology (i.e., dose-dependent vasodilation or vasoconstriction) independent of neural processing, the practical effects of these actions on neurovascular signal transmission remain relatively unknown. Because specific anesthetics may influence the specific cellular mechanisms of neurovascular elements, conducting multiple tests under different anesthesia conditions is recommended to ensure the exclusion of anesthesia confounds. This approach also helps determine the mechanisms of the generation of the signal in hemodynamic-based neuroimaging techniques.

Disclosure/conflict of interest

The authors declare no conflict of interest.

References

Akgören N, Dalgaard P, Lauritzen M (1996) Cerebral blood flow increases evoked by electrical stimulation of rat cerebellar cortex: relation to excitatory synaptic activity and nitric oxide synthesis. *Brain Res* 710:204–14

Altura BM, Altura BT, Carella A, Turlapaty PD, Weinberg J (1980) Vascular smooth muscle and general anesthetics. *Fed Proc* 39:1584–91

Ances BM, Zarahn E, Greenberg JH, Detre JA (2000) Coupling of neural activation to blood flow in the somatosensory cortex of rats is time-intensity separable, but not linear. *J Cereb Blood Flow Metab* 20:921–30

Arfors KE, Arturson G, Malmberg P (1971) Effect of prolonged chloralose anesthesia on acid-base balance and cardiovascular functions in dogs. *Acta Physiol Scand* 81:47–53

Attwell D, Buchan AM, Charpak S, Lauritzen M, Macvicar BA, Newman EA (2010) Glial and neuronal control of brain blood flow. *Nature* 468:232–43

Austin VC, Blamire AM, Allers KA, Sharp T, Styles P, Matthews PM, Sibson NR (2005) Confounding effects of anesthesia on functional activation in rodent brain: a study of halothane and alpha-chloralose anesthesia. *Neuroimage* 24:92–100

Ayata C, Dunn AK, Gursoy-OZdemir Y, Huang Z, Boas DA, Moskowitz MA (2004) Laser speckle flowmetry for the study of cerebrovascular physiology in normal and ischemic mouse cortex. *J Cereb Blood Flow Metab* 24:744–55

Berwick J, Johnston D, Jones M, Martindale J, Redgrave P, McLoughlin N, Schiessl I, Mayhew JE (2005) Neurovascular coupling investigated with two-dimensional optical imaging spectroscopy in rat whisker barrel cortex. *Eur J Neurosci* 22:1655–66

Berwick J, Martin C, Martindale J, Jones M, Johnston D, Zheng Y, Redgrave P, Mayhew J (2002) Hemodynamic response in the unanesthetized rat: intrinsic optical imaging and spectroscopy of the barrel cortex. *J Cereb Blood Flow Metab* 22:670–9

Bonvento G, Charbonné R, Corrèze JL, Borredon J, Seylaz J, Lacombe P (1994) Is alpha-chloralose plus halothane induction a suitable anesthetic regimen for cerebrovascular research? *Brain Res* 665:213–21

Boorman L, Kennerley AJ, Johnston D, Jones M, Zheng Y, Redgrave P, Berwick J (2010) Negative blood oxygen level dependence in the rat: a model for investigating the role of suppression in neurovascular coupling. *J Neurosci* 30:4285–94

Brinker G, Bock C, Busch E, Krep H, Hossmann KA, Hoehn-Berlage M (1999) Simultaneous recording of evoked potentials and T2*-weighted MR images during somatosensory stimulation of rat. *Magn Reson Med* 41:469–73

Brown CE, Boyd JD, Murphy TH (2010) Longitudinal *in vivo* imaging reveals balanced and branch-specific remodeling of mature cortical pyramidal dendritic arbors after stroke. *J Cereb Blood Flow Metab* 30:783–91

Chaigneau E, Oheim M, Audinat E, Charpak S (2003) Two-photon imaging of capillary blood flow in olfactory bulb glomeruli. *Proc Natl Acad Sci USA* 100:13081–6

Chaigneau E, Tiret P, Lecoq J, Ducros M, Knöpfel T, Charpak S (2007) The relationship between blood flow and neuronal activity in the rodent olfactory bulb. *J Neurosci* 27:6452–60

Chau PL (2010) New insights into the molecular mechanisms of general anaesthetics. *Br J Pharmacol* 161:288–307

Chen BR, Bouchard MB, McCaslin AF, Burgess SA, Hillman EM (2011) High-speed vascular dynamics of the hemodynamic response. *Neuroimage* 54:1021–30

Chen LM, Friedman RM, Ramsden BM, LaMotte RH, Roe AW (2001) Fine-scale organization of SI (area 3b) in the squirrel monkey revealed with intrinsic optical imaging. *J Neurophysiol* 86:3011–29

Chen Y, Aguirre AD, Ruvinskaya L, Devor A, Boas DA, Fujimoto JG (2009) Optical coherence tomography (OCT) reveals depth-resolved dynamics during functional brain activation. *J Neurosci Methods* 178:162–73

Colonnese MT, Phillips MA, Constantine-Paton M, Kaila K, Jasanoff A (2008) Development of hemodynamic responses and functional connectivity in rat somatosensory cortex. *Nat Neurosci* 11:72–9

Curtis DR, Lodge D (1977) Pentobarbitone enhancement of the inhibitory action of GABA. *Nature* 270:543–4

Devor A, Ulbert I, Dunn AK, Narayanan SN, Jones SR, Andermann ML, Boas DA, Dale AM (2005) Coupling of the cortical hemodynamic response to cortical and thalamic neuronal activity. *Proc Natl Acad Sci USA* 102:3822–7

Devor A, Tian P, Nishimura N, Teng IC, Hillman EM, Narayanan SN, Ulbert I, Boas DA, Kleinfeld D, Dale AM (2007) Suppressed neuronal activity and concurrent arteriolar vasoconstriction may explain negative blood oxygenation level-dependent signal. *J Neurosci* 27:4452–9

Dickinson R, Peterson BK, Banks P, Simillis C, Martin JC, Valenzuela CA, Maze M, Franks NP (2007) Competitive inhibition at the glycine site of the N-methyl-D-aspartate receptor by the anesthetics xenon and isoflurane: evidence from molecular modeling and electrophysiology. *Anesthesiology* 107:756–67

Dirnagl U, Kaplan B, Jacewicz M, Pulsinelli W (1989) Continuous measurement of cerebral cortical blood flow by laser-Doppler flowmetry in a rat stroke model. *J Cereb Blood Flow Metab* 9:589–96

Dombeck DA, Khabbaz AN, Collman F, Adelman TL, Tank DW (2007) Imaging large-scale neural activity with cellular resolution in awake, mobile mice. *Neuron* 56:43–57

Drew PJ, Shih AY, Kleinfeld D (2011) Fluctuating and sensory-induced vasodynamics in rodent cortex extend arteriole capacity. *Proc Natl Acad Sci USA* 108:8473–8

Du C, Pan Y (2011) Optical detection of brain function: simultaneous imaging of cerebral vascular response, tissue metabolism, and cellular activity *in vivo*. *Rev Neurosci* 22:695–709

Du C, Tully M, Volkow ND, Schiffer WK, Yu M, Luo Z, Koretsky AP, Benveniste H (2009) Differential effects of anesthetics on cocaine's pharmacokinetic and pharmacodynamic effects in brain. *Eur J Neurosci* 30:1565–75

Durduran T, Burnett MG, Yu G, Zhou C, Furuya D, Yodh AG, Detre JA, Greenberg JH (2004) Spatiotemporal quantification of cerebral blood flow during functional activation in rat somatosensory cortex using laser-speckle flowmetry. *J Cereb Blood Flow Metab* 24:518–25

Ebner TJ, Chen G (1995) Use of voltage-sensitive dyes and optical recordings in the central nervous system. *Prog Neurobiol* 46:463–506

Enager P, Piilgaard H, Offenhauser N, Kocharyan A, Fernandes P, Hamel E, Lauritzen M (2009) Pathway-specific variations in neurovascular and neurometabolic coupling in rat primary somatosensory cortex. *J Cereb Blood Flow Metab* 29:976–86

Fernández-Klett F, Offenhauser N, Dirnagl U, Priller J, Lindauer U (2010) Pericytes in capillaries are contractile *in vivo*, but arterioles mediate functional hyperemia in the mouse brain. *Proc Natl Acad Sci USA* 107: 22290–5

Field KJ, Lang CM (1988) Hazards of urethane (ethyl carbamate): a review of the literature. *Lab Anim* 22: 255–262

Field KJ, White WJ, Lang CM (1993) Anaesthetic effects of chloral hydrate, pentobarbitone and urethane in adult male rats. *Lab Anim* 27:258–69

Flynn N, Buljubasic N, Bosnjak ZJ, Kampine JP (1991) Cerebral vascular responses to anesthetics. *Adv Exp Med Biol* 301:237–46

Flynn NM, Buljubasic N, Bosnjak ZJ, Kampine JP (1992) Isoflurane produces endothelium-independent relaxation in canine middle cerebral arteries. *Anesthesiology* 76:461–7

Franceschini MA, Nissilä I, Wu W, Diamond SG, Bonmassar G, Boas DA (2008) Coupling between somatosensory evoked potentials and hemodynamic response in the rat. *Neuroimage* 41:189–203

Franceschini MA, Radhakrishnan H, Thakur K, Wu W, Ruvinskaya S, Carp S, Boas DA (2010) The effect of different anesthetics on neurovascular coupling. *Neuroimage* 51:1367–77

Franks NP (2008) General anaesthesia: from molecular targets to neuronal pathways of sleep and arousal. *Nat Rev Neurosci* 9:370–86

Fukuda M, Rajagopalan UM, Homma R, Matsumoto M, Nishizaki M, Tanifuji M (2005) Localization of activity-dependent changes in blood volume to submillimeter-scale functional domains in cat visual cortex. *Cereb Cortex* 15:823–33

Fuster J, Guiou M, Ardestani A, Cannestra A, Sheth S, Zhou YD, Toga A, Bodner M (2005) Near-infrared spectroscopy (NIRS) in cognitive neuroscience of the primate brain. *Neuroimage* 26:215–20

Ganjoo P, Farber NE, Hudetz A, Smith JJ, Samso E, Kampine JP, Schmeling WT (1998) *In vivo* effects of dexmedetomidine on laser-Doppler flow and pial arteriolar diameter. *Anesthesiology* 88:429–39

Garrett KM, Gan J (1998) Enhancement of gamma-aminobutyric acid A receptor activity by alpha-chloralose. *J Pharmacol Exp Ther* 285:680–6

Gerrits RJ, Raczynski C, Greene AS, Stein EA (2000) Regional cerebral blood flow responses to variable frequency whisker stimulation: an autoradiographic analysis. *Brain Res* 864:205–12

Gerrits RJ, Stein EA, Greene AS (1998) Blood flow increases linearly in rat somatosensory cortex with increased whisker movement frequency. *Brain Res* 783:151–7

Gerrits RJ, Stein EA, Greene AS (2001) Anesthesia alters NO-mediated functional hyperemia. *Brain Res* 907:20–6

Göbel W, Helmchen F (2007) *In vivo* calcium imaging of neural network function. *Physiology (Bethesda)* 22: 358–365

Gordon EL, Meno JR, Ngai AC, Lam AM, Winn HR (1995) Anesthetic-dependent pial arteriolar response to ethanol. *J Neurosurg* 83:875–7

Gu W, Jiang W, Wester P (2003) Real-time cortical cerebral blood flow follow-up in conscious, freely moving rats by laser Doppler flowmetry. *Methods* 30:172–7

Gyngell ML, Bock C, Schmitz B, Hoehn-Berlage M, Hossmann KA (1996) Variation of functional MRI signal in response to frequency of somatosensory stimulation in alpha-chloralose anesthetized rats. *Magn Reson Med* 36:13–5

Hara K, Harris RA (2002) The anesthetic mechanism of urethane: the effects on neurotransmitter-gated ion channels. *Anesth Analg* 94:313–8

Harris S, Jones M, Zheng Y, Berwick J (2010) Does neural input or processing play a greater role in the magnitude of neuroimaging signals? *Front Neuroenergetics* 2:1–7

Hayton SM, Kriss A, Muller DP (1999) Comparison of the effects of four anaesthetic agents on somatosensory evoked potentials in the rat. *Lab Anim* 33:243–51

Helmchen F (2002) Miniaturization of fluorescence microscopes using fibre optics. *Exp Physiol* 87:737–45

Hemmings Jr HC (2009) Sodium channels and the synaptic mechanisms of inhaled anaesthetics. *Br J Anaesth* 103:61–9

Hentschke H, Schwarz C, Antkowiak B (2005) Neocortex is the major target of sedative concentrations of volatile anaesthetics: strong depression of firing rates and increase of GABAA receptor-mediated inhibition. *Eur J Neurosci* 21:93–102

Hillman EM, Devor A, Bouchard MB, Dunn AK, Krauss GW, Skoch J, Bacskai BJ, Dale AM, Boas DA (2007) Depth-resolved optical imaging and microscopy of vascular compartment dynamics during somatosensory stimulation. *Neuroimage* 35:89–104

Hirano Y, Stefanovic B, Silva AC (2011) Spatiotemporal evolution of the functional magnetic resonance imaging response to ultrashort stimuli. *J Neurosci* 31:1440–7

Homma R, Baker BJ, Jin L, Garaschuk O, Konnerth A, Cohen LB, Zecevic D (2009) Wide-field and two-photon imaging of brain activity with voltage- and calcium-sensitive dyes. *Philos Trans R Soc Lond B Biol Sci* 364:2453–67

Huttunen JK, Gröhn O, Penttonen M (2008) Coupling between simultaneously recorded BOLD response and neuronal activity in the rat somatosensory cortex. *Neuroimage* 39:775–85

Hyder F, Kennan RP, Kida I, Mason GF, Behar KL, Rothman D (2000) Dependence of oxygen delivery on blood flow in rat brain: a 7 tesla nuclear magnetic resonance study. *J Cereb Blood Flow Metab* 20:485–98

Hyder F, Rothman DL, Shulman RG (2002) Total neuroenergetics support localized brain activity: implications for the interpretation of fMRI. *Proc Natl Acad Sci USA* 99:10771–6

Iadecola C (2004) Neurovascular regulation in the normal brain and in Alzheimer's disease. *Nat Rev Neurosci* 5:347–60

Iida H, Ohata H, Iida M, Watanabe Y, Dohi S (1998) Isoflurane and sevoflurane induce vasodilation of cerebral vessels via ATP-sensitive K+ channel activation. *Anesthesiology* 89:954–60

Jin T, Kim SG (2008) Cortical layer-dependent dynamic blood oxygenation, cerebral blood flow and cerebral blood volume responses during visual stimulation. *Neuroimage* 43:1–9

Jones M, Berwick J, Johnston D, Mayhew J (2001) Concurrent optical imaging spectroscopy and laser-Doppler flowmetry: the relationship between blood flow, oxygenation, and volume in rodent barrel cortex. *Neuroimage* 13:1002–15

Jukovskaya N, Tiret P, Lecoq J, Charpak S (2011) What does local functional hyperemia tell about local neuronal activation? *J Neurosci* 31:1579–82

Kannurpatti SS, Biswal BB (2006) Spatial extent of CBF response during whisker stimulation using trial averaged laser Doppler imaging. *Brain Res* 1089:135–42

Kannurpatti SS, Biswal BB (2011) Frequency tuning in the rat whisker barrel cortex revealed through RBC flux maps. *Brain Res* 1417:16–26

Keilholz SD, Silva AC, Raman M, Merkle H, Koretsky AP (2004) Functional MRI of the rodent somatosensory pathway using multislice echo planar imaging. *Magn Reson Med* 52:89–99

Keller CJ, Cash SS, Narayanan S, Wang C, Kuzniecky R, Carlson C, Devinsky O, Thesen T, Doyle W, Sassaroli A, Boas DA, Ulbert I, Halgren E (2009) Intracranial microprobe for evaluating neuro-hemodynamic coupling in unanesthetized human neocortex. *J Neurosci Methods* 179:208–18

Khananashvili YA, Demidova AA (2002) Dynamics of the development of microvascular reactions in the projection zones of the somatosensory cortex of the brain in rats. *Neurosci Behav Physiol* 32:435–42

Kim T, Hendrich KS, Masamoto K, Kim SG (2007) Arterial versus total blood volume changes during neural activity-induced cerebral blood flow change: implication for BOLD fMRI. *J Cereb Blood Flow Metab* 27: 1235–1247

Kim T, Masamoto K, Fukuda M, Vazquez A, Kim SG (2010) Frequency-dependent neural activity, CBF, and BOLD fMRI to somatosensory stimuli in isoflurane-anesthetized rats. *Neuroimage* 52:224–33

Kleinfeld D, Blinder P, Drew PJ, Driscoll JD, Muller A, Tsai PS, Shih AY (2011) A guide to delineate the logic of neurovascular signaling in the brain. *Front Neuroenergetics* 3:1–9

Kleinfeld D, Mitra PP, Helmchen F, Denk W (1998) Fluctuations and stimulus-induced changes in blood flow observed in individual capillaries in layers 2 through 4 of rat neocortex. *Proc Natl Acad Sci USA* 95:15741–6

Krautwald K, Angenstein F (2012) Low frequency stimulation of the perforant pathway generates anesthesia-specific variations in neural activity and BOLD responses in the rat dentate gyrus. *J Cereb Blood Flow Metab* 32:291–305

Kuschinsky W, Suda S, Sokoloff L (1985) Influence of gamma-hydroxybutyrate on the relationship between local cerebral glucose utilization and local cerebral blood flow in the rat brain. *J Cereb Blood Flow Metab* 5: 58–64

Lahti KM, Ferris CF, Li F, Sotak CH, King JA (1998) Imaging brain activity in conscious animals using functional MRI. *J Neurosci Methods* 82:75–83

Lahti KM, Ferris CF, Li F, Sotak CH, King JA (1999) Comparison of evoked cortical activity in conscious and propofol-anesthetized rats using functional MRI. *Magn Reson Med* 41:412–6

Lauritzen M (2001) Relationship of spikes, synaptic activity, and local changes of cerebral blood flow. *J Cereb Blood Flow Metab* 21:1367–83

Lecrux C, Toussay X, Kocharyan A, Fernandes P, Neupane S, Lévesque M, Plaisier F, Shmuel A, Cauli B, Hamel E (2011) Pyramidal neurons are "neurogenic hubs" in the neurovascular coupling response to whisker stimulation. *J Neurosci* 31:9836–47

Lee JG, Hudetz AG, Smith JJ, Hillard CJ, Bosnjak ZJ, Kampine JP (1994) The effects of halothane and isoflurane on cerebrocortical microcirculation and autoregulation as assessed by laser-Doppler flowmetry. *Anesth Analg* 79:58–65

Lee JG, Smith JJ, Hudetz AG, Hillard CJ, Bosnjak ZJ, Kampine JP (1995) Laser-Doppler measurement of the effects of halothane and isoflurane on the cerebrovascular CO2 response in the rat. *Anesth Analg* 80:696–702

Lee SP, Duong TQ, Yang G, Iadecola C, Kim SG (2001) Relative changes of cerebral arterial and venous blood volumes during increased cerebral blood flow: implications for BOLD fMRI. *Magn Reson Med* 45:791–800

Leniger-Follert E, Hossmann KA (1979) Simultaneous measurements of microflow and evoked potentials in the somatomotor cortex of the cat brain during specific sensory activation. *Pflugers Arch* 380:85–9

Lenz C, Rebel A, van Ackern K, Kuschinsky W, Waschke KF (1998) Local cerebral blood flow, local cerebral glucose utilization, and flow-metabolism coupling during sevoflurane versus isoflurane anesthesia in rats. *Anesthesiology* 89:1480–8

Lincoln DW (1969) Correlation of unit activity in the hypothalamus with EEG patterns associated with the sleep cycle. *Exp Neurol* 24:1–18

Lindauer U, Villringer A, Dirnagl U (1993) Characterization of CBF response to somatosensory stimulation: model and influence of anesthetics. *Am J Physiol* 264:H1223–8

Logothetis NK, Pauls J, Augath M, Trinath T, Oeltermann A (2001) Neurophysiological investigation of the basis of the fMRI signal. *Nature* 412:150–7

Lukasik VM, Gillies RJ (2003) Animal anaesthesia for *in vivo* magnetic resonance. *NMR Biomed* 16:459–67

Maekawa T, Tommasino C, Shapiro HM, Keifer-Goodman J, Kohlenberger RW (1986) Local cerebral blood flow and glucose utilization during isoflurane anesthesia in the rat. *Anesthesiology* 65:144–51

Maggi CA, Meli A (1986) Suitability of urethane anesthesia for physiopharmacological investigations in various systems. Part 1: General considerations. *Experientia* 42:109–14

Maheswari RU, Takaoka H, Kadono H, Homma R, Tanifuji M (2003) Novel functional imaging technique from brain surface with optical coherence tomography enabling visualization of depth resolved functional structure *in vivo*. *J Neurosci Methods* 124:83–92

Mantz J, Cordier J, Giaume C (1993) Effects of general anesthetics on intercellular communications mediated by gap junctions between astrocytes in primary culture. *Anesthesiology* 78:892–901

Martin C, Berwick J, Johnston D, Zheng Y, Martindale J, Port M, Redgrave P, Mayhew J (2002) Optical imaging spectroscopy in the unanaesthetised rat. *J Neurosci Methods* 120:25–34

Martin C, Martindale J, Berwick J, Mayhew J (2006) Investigating neural- hemodynamic coupling and the hemodynamic response function in the awake rat. *Neuroimage* 32:33–48

Martindale J, Mayhew J, Berwick J, Jones M, Martin C, Johnston D, Redgrave P, Zheng Y (2003) The hemodynamic impulse response to a single neural event. *J Cereb Blood Flow Metab* 23:546–55

Masamoto K, Fukuda M, Vazquez A, Kim SG (2009) Dose-dependent effect of isoflurane on neurovascular coupling in rat cerebral cortex. *Eur J Neurosci* 30:242–50

Masamoto K, Kim T, Fukuda M, Wang P, Kim SG (2007) Relationship between neural, vascular, and BOLD signals in isoflurane-anesthetized rat somatosensory cortex. *Cereb Cortex* 17:942–50

Masamoto K, Obata T, Kanno I (2010**a**) Cerebrovascular dynamics in response to neural stimulation. *Hirosaki Med J* 61:S181–6

Masamoto K, Obata T, Kanno I (2010**b**) Intracortical microcirculatory change induced by anesthesia in rat somatosensory cortex. *Adv Exp Med Biol* 662:57–61

Matsuura T, Fujita H, Kashikura K, Kanno I (2000) Evoked local cerebral blood flow induced by somatosensory stimulation is proportional to the baseline flow. *Neurosci Res* 38:341–8

Matsuura T, Fujita H, Seki C, Kashikura K, Kanno I (1999) Hemodynamics evoked by microelectrical direct stimulation in rat somatosensory cortex. *Comp Biochem Physiol A Mol Integr Physiol* 124:47–52

Matsuura T, Kanno I (2001) Quantitative and temporal relationship between local cerebral blood flow and neuronal activation induced by somatosensory stimulation in rats. *Neurosci Res* 40:281–90

Minchin MC (1981) The effect of anaesthetics on the uptake and release of gamma-aminobutyrate and D-aspartate in rat brain slices. *Br J Pharmacol* 73:681–9

Miyazaki H, Nakamura Y, Arai T, Kataoka K (1997) Increase of glutamate uptake in astrocytes: a possible mechanism of action of volatile anesthetics. *Anesthesiology* 86: 1359–66

Moskalenko YE, Dowling JL, Liu D, Rovainen CM, Semernia VN, Woolsey TA (1996) LCBF changes in rat somatosensory cortex during whisker stimulation monitored by dynamic H2 clearance. *Int J Psychophysiol* 21: 45–59

Nakamura K, Terasako K, Toda H, Miyawaki I, Kakuyama M, Nishiwada M, Hatano Y, Mori K (1994) Mechanisms of inhibition of endothelium-dependent relaxation by halothane, isoflurane, and sevoflurane. *Can J Anaesth* 41:340–6

Nakao Y, Itoh Y, Kuang TY, Cook M, Jehle J, Sokoloff L (2001) Effects of anesthesia on functional activation of cerebral blood flow and metabolism. *Proc Natl Acad Sci USA* 98:7593–8

Ngai AC, Jolley MA, D'Ambrosio R, Meno JR, Winn HR (1999) Frequency-dependent changes in cerebral blood flow and evoked potentials during somatosensory stimulation in the rat. *Brain Res* 837:221–8

Nicoll RA (1978) Pentobarbital: differential postsynaptic actions on sympathetic ganglion cells. *Science* 199: 451–2

Nielsen NA, Lauritzen M (2001) Coupling and uncoupling of activity-dependent increases of neuronal activity and blood flow in rat somatosensory cortex. *J Physiol* 533:773–85

Obrenovitch TP, Chen S, Farkas E (2009) Simultaneous, live imaging of cortical spreading depression and associated cerebral blood flow changes, by combining voltage-sensitive dye and laser speckle contrast methods. *Neuroimage* 45:68–74

Obrig H, Villringer A (2003) Beyond the visible–imaging the human brain with light. *J Cereb Blood Flow Metab* 23:1–18

Ogawa S, Lee TM, Stepnoski R, Chen W, Zhu XH, Ugurbil K (2000) An approach to probe some neural systems interaction by functional MRI at neural time scale down to milliseconds. *Proc Natl Acad Sci USA* 97:11026–31

Ogura K, Takayasu M, Dacey Jr RG (1991) Differential effects of pentobarbital on intracerebral arterioles and venules of rats *in vitro*. *Neurosurgery* 28:537–41

Otsuka T, Wei L, Acuff VR, Shimizu A, Pettigrew KD, Patlak CS, Fenstermacher JD (1991) Variation in local cerebral blood flow response to high-dose pentobarbital sodium in the rat. *Am J Physiol* 261:H110–20

Ou W, Nissilä I, Radhakrishnan H, Boas DA, Hämäläinen MS, Franceschini MA (2009) Study of neurovascular coupling in humans via simultaneous magnetoencephalography and diffuse optical imaging acquisition. *Neuroimage* 46:624–32

Pawela CP, Biswal BB, Hudetz AG, Schulte ML, Li R, Jones SR, Cho YR, Matloub HS, Hyde JS (2009) A protocol for use of medetomidine anesthesia in rats for extended studies using task-induced BOLD contrast and resting-state functional connectivity. *Neuroimage* 46:1137–47

Peeters RR, Tindemans I, De Schutter E, Van der Linden A (2001) Comparing BOLD fMRI signal changes in the awake and anesthetized rat during electrical forepaw stimulation. *Magn Reson Imaging* 19:821–6

Reinert H (1964) Urethane hyperclycaemia and hypothalamic activation. *Nature* 204:889–91

Reinert KC, Gao W, Chen G, Ebner TJ (2007) Flavoprotein autofluorescence imaging in the cerebellar cortex *in vivo*. *J Neurosci Res* 85:3221–32

Rosengarten B, Kaps M (2010) A simultaneous EEG and transcranial Doppler technique to investigate the neurovascular coupling in the human visual cortex. *Cerebrovasc Dis* 29:211–6

Sandman CA, O'Halloran JP, Isenhart R (1984) Is there an evoked vascular response? *Science* 224:1355–7

Sándor P, Nyáry I, Reivich M, Kovách AG (1977) Comparative effects of chloralose anesthesia and Sernylan analgesia on cerebral blood flow, CO2 responsiveness, and brain metabolism in the baboon. *Stroke* 8:432–6

Sandstrom DJ (2004) Isoflurane depresses glutamate release by reducing neuronal excitability at the Drosophila neuromuscular junction. *J Physiol* 558:489–502

Sanganahalli BG, Herman P, Hyder F (2008) Frequency-dependent tactile responses in rat brain measured by functional MRI. *NMR Biomed* 21:410–6

Schregardus DS, Pieneman AW, Ter Maat A, Jansen RF, Brouwer TJ, Gahr ML (2006) A lightweight telemetry system for recording neuronal activity in freely behaving small animals. *J Neurosci Methods* 155:62–71

Schulte ML, Hudetz AG (2006) Functional hyperemic response in the rat visual cortex under halothane anesthesia. *Neurosci Lett* 394:63–8

Sebel PS, Ingram DA, Flynn PJ, Rutherfoord CF, Rogers H (1986) Evoked potentials during isoflurane anaesthesia. *Br J Anaesth* 58:580–5

Seylaz J, Charbonné R, Nanri K, Von Euw D, Borredon J, Kacem K, Méric P, Pinard E (1999) Dynamic *in vivo* measurement of erythrocyte velocity and flow in capillaries and of microvessel diameter in the rat brain by confocal laser microscopy. *J Cereb Blood Flow Metab* 19:863–70

Sheth S, Nemoto M, Guiou M, Walker M, Pouratian N, Toga AW (2003) Evaluation of coupling between optical intrinsic signals and neuronal activity in rat somatosensory cortex. *Neuroimage* 19:884–94

Sheth SA, Nemoto M, Guiou M, Walker M, Pouratian N, Toga AW (2004) Linear and nonlinear relationships between neuronal activity, oxygen metabolism, and hemodynamic responses. *Neuron* 42:347–55

Sheth SA, Nemoto M, Guiou MW, Walker MA, Toga AW (2005) Spatiotemporal evolution of functional hemodynamic changes and their relationship to neuronal activity. *J Cereb Blood Flow Metab* 25:830–41

Shibuki K, Hishida R, Murakami H, Kudoh M, Kawaguchi T, Watanabe M, Watanabe S, Kouuchi T, Tanaka R (2003) Dynamic imaging of somatosensory cortical activity in the rat visualized by flavoprotein autofluorescence. *J Physiol* 549:919–27

Shtoyerman E, Arieli A, Slovin H, Vanzetta I, Grinvald A (2000) Long-term optical imaging and spectroscopy reveal mechanisms underlying the intrinsic signal and stability of cortical maps in V1 of behaving monkeys. *J Neurosci* 20:8111–21

Shulman RG, Rothman DL, Hyder F (1999) Stimulated changes in localized cerebral energy consumption under anesthesia. *Proc Natl Acad Sci USA* 96:3245–50

Sicard K, Shen Q, Brevard ME, Sullivan R, Ferris CF, King JA, Duong TQ (2003) Regional cerebral blood flow and BOLD responses in conscious and anesthetized rats under basal and hypercapnic conditions: implications for functional MRI studies. *J Cereb Blood Flow Metab* 23:472–81

Silva AC, Koretsky AP (2002) Laminar specificity of functional MRI onset times during somatosensory stimulation in rat. *Proc Natl Acad Sci USA* 99:15182–7

Silva AC, Lee SP, Yang G, Iadecola C, Kim SG (1999) Simultaneous blood Oxygenation level-dependent and cerebral blood flow functional magnetic resonance imaging during forepaw stimulation in the rat. *J Cereb Blood Flow Metab* 19:871–9

Silva AC, Lee SP, Iadecola C, Kim SG (2000) Early temporal characteristics of cerebral blood flow and deoxyhemoglobin changes during somatosensory stimulation. *J Cereb Blood Flow Metab* 20:201–6

Silverman J, Muir III WW (1993) A review of laboratory animal anesthesia with chloral hydrate and chloralose. *Lab Anim Sci* 43:210–6

Sinclair MD (2003) A review of the physiological effects of alpha2-agonists related to the clinical use of medetomidine in small animal practice. *Can Vet J* 44:885–97

Smith AJ, Blumenfeld H, Behar KL, Rothman DL, Shulman RG, Hyder F (2002) Cerebral energetics and spiking frequency: the neurophysiological basis of fMRI. *Proc Natl Acad Sci USA* 99:10765–70

Sun X, Wang Y, Chen S, Luo W, Li P, Luo Q (2011) Simultaneous monitoring of intracellular pH changes and hemodynamic response during cortical spreading depression by fluorescence-corrected multimodal optical imaging. *Neuroimage* 57:873–84

Takano T, Tian GF, Peng W, Lou N, Libionka W, Han X, Nedergaard M (2006) Astrocyte-mediated control of cerebral blood flow. *Nat Neurosci* 9:260–7

Takashima I, Kajiwara R, Iijima T (2001) Voltage-sensitive dye versus intrinsic signal optical imaging: comparison of optically determined functional maps from rat barrel cortex. *Neuroreport* 12:2889–94

Takuwa H, Autio J, Nakayama H, Matsuura T, Obata T, Okada E, Masamoto K, Kanno I (2011) Reproducibility and variance of a stimulation-induced hemodynamic response in barrel cortex of awake behaving mice. *Brain Res* 1369:103–11

Tanaka K, Kawano T, Tsutsumi YM, Kinoshita M, Kakuta N, Hirose K, Kimura M, Oshita S (2011) Differential effects of propofol and isoflurane on glucose utilization and insulin secretion. *Life Sci* 88:96–103

Tétrault S, Chever O, Sik A, Amzica F (2008) Opening of the blood-brain barrier during isoflurane anaesthesia. *Eur J Neurosci* 28:1330–41

Tian P, Teng IC, May LD, Kurz R, Lu K, Scadeng M, Hillman EM, De Crespigny AJ, D'Arceuil HE, Mandeville JB, Marota JJ, Rosen BR, Liu TT, Boas DA, Buxton RB, Dale AM, Devor A (2010) Cortical depth-specific microvascular dilation underlies laminar differences in blood oxygenation level-dependent functional MRI signal. *Proc Natl Acad Sci USA* 107:15246–51

Toda H, Nakamura K, Hatano Y, Nishiwada M, Kakuyama M, Mori K (1992) Halothane and isoflurane inhibit endothelium-dependent relaxation elicited by acetylcholine. *Anesth Analg* 75:198–203

Tomita Y, Kubis N, Calando Y, Tran Dinh A, Méric P, Seylaz J, Pinard E (2005) Long-term *in vivo* investigation of mouse cerebral microcirculation by fluorescence confocal microscopy in the area of focal ischemia. *J Cereb Blood Flow Metab* 25:858–67

Tsuji T, Chiba S (1987) Mechanism of vascular responsiveness to barbiturates in isolated and perfused canine basilar arteries. *Neurosurgery* 21:161–6

Tung A, Herrera S, Fornal CA, Jacobs BL (2008) The effect of prolonged anesthesia with isoflurane, propofol, dexmedetomidine, or ketamine on neural cell proliferation in the adult rat. *Anesth Analg* 106:1772–7

Ueki M, Mies G, Hossmann KA (1992) Effect of alpha-chloralose, halothane, pentobarbital and nitrous oxide anesthesia on metabolic coupling in somatosensory cortex of rat. *Acta Anaesthesiol Scand* 36:318–22

Van Aken H, van Hemelrijck J (1991) Influence of anesthesia on cerebral blood flow and cerebral metabolism: an overview. *Agressologie* 32:303–6

Van Camp N, Verhoye M, Van der Linden A (2006) Stimulation of the rat somatosensory cortex at different frequencies and pulse widths. *NMR Biomed* 19:10–7

Vanzetta I, Grinvald A (2008) Coupling between neuronal activity and microcirculation: implications for functional brain imaging. *HFSP J* 2:79–98

Villringer A, Dirnagl U (1995) Coupling of brain activity and cerebral blood flow: basis of functional neuroimaging. *Cerebrovasc Brain Metab Rev* 7:240–76

Villringer A, Them A, Lindauer U, Einhäupl K, Dirnagl U (1994) Capillary perfusion of the rat brain cortex. An *in vivo* confocal microscopy study. *Circ Res* 75:55–62

Violet JM, Downie DL, Nakisa RC, Lieb WR, Franks NP (1997) Differential sensitivities of mammalian neuronal and muscle nicotinic acetylcholine receptors to general anesthetics. *Anesthesiology* 86:866–74

Vogel J, Kuschinsky W (1996) Decreased heterogeneity of capillary plasma flow in the rat whisker-barrel cortex during functional hyperemia. *J Cereb Blood Flow Metab* 16:1300–6

Wang K, Zheng C, Wu C, Gao M, Liu Q, Yang K, Ellsworth K, Xu L, Wu J (2008) alpha-Chloralose diminishes gamma oscillations in rat hippocampal slices. *Neurosci Lett* 441:66–71

Weber B, Burger C, Wyss MT, von Schulthess GK, Scheffold F, Buck A (2004) Optical imaging of the spatiotemporal dynamics of cerebral blood flow and oxidative metabolism in the rat barrel cortex. *Eur J Neurosci* 20:2664–70

Weber R, Ramos-Cabrer P, Wiedermann D, van Camp N, Hoehn M (2006) A fully noninvasive and robust experimental protocol for longitudinal fMRI studies in the rat. *Neuroimage* 29:1303–10

Wei L, Otsuka T, Acuff V, Bereczki D, Pettigrew K, Patlak C, Fenstermacher J (1993) The velocities of red cell and plasma flows through parenchymal microvessels of rat brain are decreased by pentobarbital. *J Cereb Blood Flow Metab* 13:487–97

Williams KA, Magnuson M, Majeed W, LaConte SM, Peltier SJ, Hu X, Keilholz SD (2010) Comparison of alpha-chloralose, medetomidine and isoflurane anesthesia for functional connectivity mapping in the rat. *Magn Reson Imaging* 28:995–1003

Wu XS, Sun JY, Evers AS, Crowder M, Wu LG (2004) Isoflurane inhibits transmitter release and the presynaptic action potential. *Anesthesiology* 100:663–670

Zhao F, Zhao T, Zhou L, Wu Q, Hu X (2008) BOLD study of stimulation-induced neural activity and resting-state connectivity in medetomidine-sedated rat. *Neuroimage* 39:248–60

3D Analysis of Intracortical Microvasculature during Chronic Hypoxia in Mouse Brains

Kouichi Yoshihara[1], Hiroyuki Takuwa[2], Iwao Kanno[2], Shinpei Okawa[1], Yukio Yamada[1] and Kazuto Masamoto[2,3]

[1]Department of Mechanical Engineering and Intelligent Systems, University of Electro-Communications, Japan, [2]Molecular Imaging Center, National Institute of Radiological Sciences, Japan, [3]Center for Frontier Science and Engineering, University of Electro-Communications, Japan

Abstract The purpose of this study is to determine when and where the brain microvasculature changes its network in response to chronic hypoxia. To identify the hypoxia-induced structural adaptation, we longitudinally imaged cortical microvasculature at the same location within a mouse somatosensory cortex with two-photon microscopy repeatedly for up to one month during continuous exposure to hypoxia (either 8% or 10% oxygen conditions). The two-photon microscopy approach made it possible to track a 3D pathway from a cortical surface arteriole to a venule up to a depth of 0.8 mm from the cortical surface. The network pathway was then divided into individual vessel segments at the branches, and their diameters and lengths were measured. We observed 3 to 11 vessel segments between the penetrating arteriole and the emerging vein over the depths of 20 to 460 μm within the 3D reconstructed image (0.46 x 0.46 x 0.80 mm^3). The average length of the individual capillaries (< 7 μm in diameter) was 67 ± 46 μm, which was not influenced by hypoxia. In contrast, 1.4 ± 0.3 and 1.2 ± 0.2 fold increases of the capillary diameter were observed 1 week after exposure to 8% and 10% hypoxia, respectively. At 3 weeks from the exposure, the capillary diameter reached 8.5 ± 1.9 μm and 6.7 ± 1.8 μm in 8% and 10% hypoxic conditions, respectively, which accounted for the 1.8 ± 0.5 and 1.4 ± 0.3 fold increases relative to those of the prehypoxic condition. The vasodilation of penetrating arterioles (1.4 ± 0.2 and 1.2 ± 0.2 fold increases) and emerging veins (1.3 ± 0.2 and 1.3 ± 0.2 fold increases) showed relatively small diameter changes compared with the parenchymal capillaries. These findings indicate that parenchymal capillaries are the major site responding to the oxygen environment during chronic hypoxia.

1 Introduction

The brain is known to be an organ vulnerable to a lack of oxygen. Only 2 to 3 minutes without an adequate oxygen supply leads to irreversible damage of central

nervous system (CNS) functions. To maintain an adequate supply, the brain vasculature is well organized to allow the diffusion of oxygen to every region of the tissue[1]. Previous studies have shown that the density of brain microvessels adaptively increased in response to chronic hypoxia[2,3]. Angiogenesis and degeneration of the microvasculature were also reported in response to a progress of brain tumors and Alzheimer's disease, respectively[4,5]. These studies strongly indicate that close interaction exists between brain microvasculature and tissue activity to maintain an adequate supply of oxygen. However, the mechanism that regulates the brain microvasculature and its effect on tissue oxygen homeostasis remains mostly unknown.

Because one of the reasons for the lack of knowledge about the structural adaptations of brain microvasculature is a lack of longitudinal studies at the capillary network scale, here, we longitudinally tracked the spatial and temporal adaptation of the microvasculature during chronic hypoxia in a mouse somatosensory cortex with two-photon microscopy. The same three-dimensional (3D) microvasculature was imaged every week for up to one month during continuous exposure to hypoxia (at either 8% or 10% oxygen). Two-photon microscopy is based on the principle of nonlinear optics[6,7,8]. In addition, two-photon microscopy allows excitation with near-infrared light, which has the advantage of providing a long penetration depth in biological tissues[9]. In the present study, volume images of the cortical microvasculature were captured up to a depth of 0.8 mm from the cortical surface with a step size of 0.005 mm and reconstructed with 3D rendering. The 3D pathways of the parenchymal microvasculature were identified and divided into individual segments at the branches. The diameters and lengths of the segments were measured, and their temporal changes were longitudinally traced over the periods of the measurements. Finally, the surface areas and volumes of the vessel segments were calculated to evaluate the adaptation of the microvasculature.

2 Materials and Methods

2.1 Image Analysis

The 3D image (field of view: 0.46×0.46×0.80 mm^3) consists of approximately 160 2D images in the x-y plane parallel to the brain surface with a depth step of 5 μm, and each 2D image has 1024×1024 pixels with an individual pixel size of 0.45 μm. The image analysis performed in each step is described below.

(i) Identification of parenchymal arteriovenous pathway

One target pathway between a surface artery and a vein through parenchymal microvasculature was identified within the reconstructed image (Figs. 1a,b), by

tracking all branches from the artery to the vein including penetrating arterioles, parenchymal capillaries (< 7 μm in diameter), and emerging veins.

(ii) Segmentation of vessels

The vessel segments in the pathway were sequentially numbered (Fig. 1c). One vessel segment was defined as the vessel having two-branches at both ends. The sequential numbers were assigned, beginning from the penetrating artery and ending with the emerging vein.

(iii) Measurement of the length of a vessel segment

The vessel length was measured as the distance from one end to the other end along the centerline of the vessel segment. Several measurement points were manually placed on the centerline to account for the curvature of the vessel. By summing all the distances between the neighboring two measuring points, the vessel length was obtained.

(iv) Measurement of the vessel diameter

The vessel diameter was measured as the average of the diameters at 10 different positions in the vessel segment. Because the intensity differences (i.e., contrast) in the images were sufficient to discriminate the vessel edges relative to the tissue, it was not difficult to manually assign the edges of the vessels to measure the vessel diameters (Fig. 1d).

(v) Calculation of the vessel surface area and volume

The surface areas and volumes of each vessel segment were calculated from the measured diameters and lengths by assuming that each vessel segment was approximated as a cylinder.

2.2. Animal experiments

All experimental protocols were approved by the Institutional Animal Care and Use Committee of the National Institute of Radiological Sciences and the University of Electro-Communications, and the experiments were conducted by following the approved protocols. Ten male C57BL/6J mice (21–23 g) were randomly divided into two groups: one for the 8% oxygen experiment (n=5) and the other for the 10% oxygen experiment (n=5). A custom-made fixation device was fixed to the animal's head for two-photon microscopy imaging[10]. At 2 weeks post-operation, the experiments with hypoxic exposure initiated. During the imaging experiments, the mice were anesthetized with isoflurane (1%) in a mixture of air and oxygen gas, and their rectal temperature was maintained at 37±1°C. Sulforhodamine 101 (SR101) dissolved in saline (5 mM) was intraperitoneally injected into the animal (8 mL/kg) for labeling blood plasma, and cortical vasculature was imaged with a two-photon microscope (TCS SP5MP, Leica Microsystems, Germany) equipped with a Ti:Sapphire laser (MaiTai HP, Spectra-Physics, CA). The excitation wavelength was 900 nm (average power 2.0 W output), and the emission signal was detected through a bandpass filter (610/75 nm).

At day 0 (start of exposure to hypoxia), a reference image of the cortical surface vasculature was obtained with reflection acquisition mode excited at 633 nm with a low magnification object lens (field of view: 3.6×3.6 mm^2). The cortical arteries and veins were distinguished in the reflection image; the arteries and veins exhibited different light intensities because of their different light absorption characteristics[9]. Because the pattern of the cortical surface vessels was preserved over the period of the longitudinal experiments, the reference image was used to identify the measurement locations at different imaging experiments. Except while undergoing imaging, the animals were kept in either an 8% or 10% oxygen room in which the oxygen level was monitored with an oxygen sensor. The imaging experiments were repeatedly performed on days 0, 7, 14, 21, and 31 after exposure to hypoxia. Because 3 out of 5 animals were dead after 3 weeks in the 8% oxygen experiment, the analytical results were only compared for the first 3 weeks of measurements. Data were represented as mean ± standard deviation.

3. Results and Discussion

Reconstructed 3D images of cortical microvasculature are represented in Fig. 2. The images show the apparently same 3D structures over the period of one month during continuous exposure to hypoxia. The 3D pathways were identified from penetrating arteriole (A) to emerging vein (V) through parenchymal capillaries (C), which had 5 to 13 branches between the surface artery and the vein over depths of 20 to 460 μm within the image. The total length from the beginning of a penetrating arteriole to the end point of the emerging vein was 703 ± 278 μm (311 -1221 μm, n=30 networks), which was unchanged during chronic hypoxia over 3 weeks (Table 1). In contrast, the parenchymal capillary diameter was predominantly increased by 1.4 ± 0.3 and 1.2 ± 0.2 fold at 1 week after continuous exposure to 8% and 10% oxygen, respectively (Table 1). The vasodilation of parenchymal capillaries continued over 3 weeks: 1.8 ± 0.5 and 1.4 ± 0.3 fold relative to that of the prehypoxic condition. This increase was significantly higher than both the penetrating arterioles (1.4 ± 0.2 times) and emerging veins (1.3 ± 0.2 times) under the 8% oxygen condition but not the 10% oxygen condition (1.2 ± 0.2 fold for arterioles and 1.3 ± 0.2 fold for veins). Consequently, the vessel surface area increased by 1.5 ± 0.4, 1.8 ± 0.7, and 1.2 ± 0.3 fold for arterioles, capillaries, and veins after 3 weeks under 8% oxygen exposure and by 1.2 ± 0.3, 1.4 ± 0.5, and 1.3 ± 0.3 fold for 10% oxygen, respectively. In addition, the vessel volume was 2.1 ± 0.9, 3.5 ± 2.5, and 1.7 ± 0.6 times larger for 8% oxygen and 1.6 ± 0.5, 2.1 ± 1.6, and 1.6 ± 0.6 times larger for 10% oxygen. These results show that depending on the level of hypoxia, vascular restructuring was induced for different vessel types. In particular, the lower oxygen level (8%) caused a predominant increase in the parenchymal capillary volumes, indicating that several mechanisms may be participating in the hypoxia-induced restructuring of cortical microvasculature. Future studies are needed to investigate the mechanism

of oxygen level sensing and the driving force leading to a change in the capillary diameter to further understand the mechanism involved in maintaining tissue oxygen homeostasis in the brain.

4. Conclusions

The present study quantified hypoxia-induced restructuring of cerebral microvasculature based on 3D network pathways measured with two-photon microscopy at the same locations within mouse brains over one month. We found that hypoxia-induced vasodilation occurred predominantly in the parenchymal capillaries, indicating that parenchymal capillaries are the major site responding to the chronic hypoxic environment.

Acknowledgments The authors thank Mr. Ryutaro Asaga and Mr. Ryota Sakamoto for their help in the preparation of the experiments. This work was partially supported by Special Coordination Funds for Promoting Science and Technology (K.M.).

References

1. Masamoto K, Tanishita K (2009) Oxygen transport in brain tissue. J Biomech Eng 131: 074002
2. Boero JA, Ascher J, Arregui A et al (1999) Increased brain capillaries in chronic hypoxia. J Appl Physiol 86:1211-1219
3. Xu K, LaManna JC (2006) Chronic hypoxia and the cerebral circulation. J Appl Physiol 100:725-730
4. Wsseling P, Ruiter DJ, Burger PC (1997) Angiogenesis in brain tumors; pathobiological and clinical aspects. J Neurooncol 32:253-265
5. Meyer EP, Ulmann-Schuler A, Staufenbiel M et al (2008) Altered morphology and 3D architecture of brain vasculature in a mouse mode for Alzheimer's disease. Proc Natl Acad Sci U S A 105:3587-3592
6. Denk W, Strickler JH, Webb WW (1990) Two-photon laser scanning fluorescence microscopy. Science 248:73-76
7. So PT, Dong CY, Masters BR et al (2000) Two-photon excitation fluorescence microscopy. Annu Rev Biomed Eng 2:399-429
8. Helmchen F, Denk W (2005) Deep tissue two-photon microscopy. Nat Methods 2:932-940
9. Yamada Y (1995) Light-tissue interaction and optical imaging in biomedicine. Annual Review of Heat Transfer (Begell house, Inc.) 6:1-59
10. Takuwa H, Autio J, Nakayama H et al (2011) Reproducibility and variance of a stimulation-induced hemodynamic response in barrel cortex of awake behaving mice. Brain Res 1369: 103-111

Table 1 Vessel diameter and length measurements of single pathways from a penetrating arteriole (A) to the emerging vein (V) through parenchymal capillaries (C, < 7 μm in diameter) during chronic hypoxia

i) 8% O_2 (n=5)

	Diameter (μm)				Length (μm)			
(total #)	day 0	day 7	day 14	day 21	day 0	day 7	day 14	day 21
A (32)	11±5	14±5	15±5	16±6	77±41	78±39	76±41	77±38
C (61)	4.9±0.9	6.8±1.3	7.5±1.7	8.5±1.9	68±48	69±49	67±46	67±46
V (23)	17±9	21±10	23±12	23±13	91±69	88±66	86±61	81±58

ii) 10% O_2 (n=5)

	Diameter (μm)				Length (μm)			
(total #)	day 0	day 7	day 14	day 21	day 0	day 7	day 14	day 21
A (42)	14±6	17±7	18±7	18±7	126±108	123±108	122±106	123±106
C (69)	5.0±1.0	5.9±1.4	6.4±1.5	6.7±1.8	61±37	62±36	60±36	61±35
V (21)	17±8	19±8	20±9	21±10	136±127	141±122	134±121	133±119

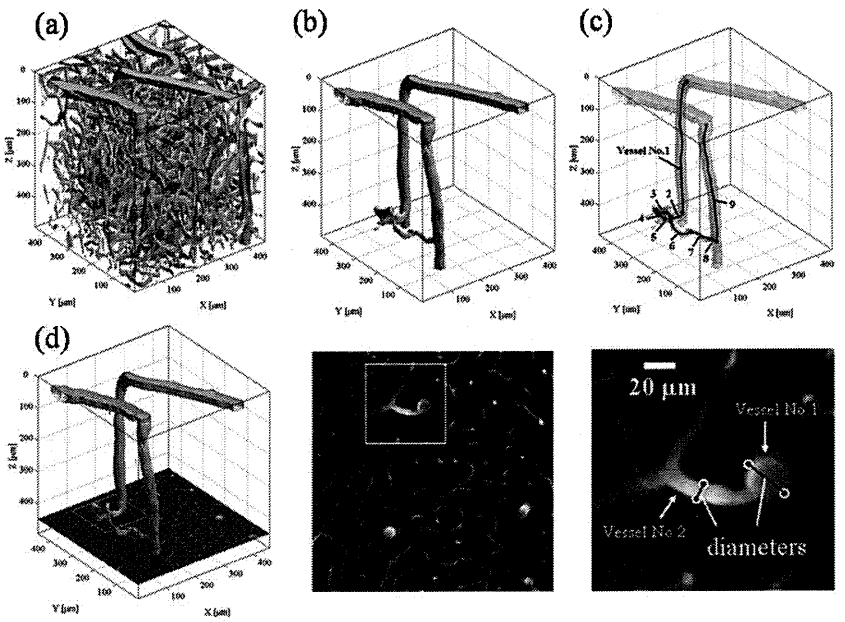

Figure 1. Methods for measuring vessel diameter and length. (a) Reconstructed volume image of parenchymal microvasculature; binarized from 3D image that was reconstructed by rendering obtained 2D x-y images. (b) Selection of a single vessel pathway; the selection criterion was to have the entire connection from the surface arteriole to the surface venule visible within the image. (c) Segmentation and measurement of the length of individual vessel segments. (d) Manual measurement of vessel diameter in the image.

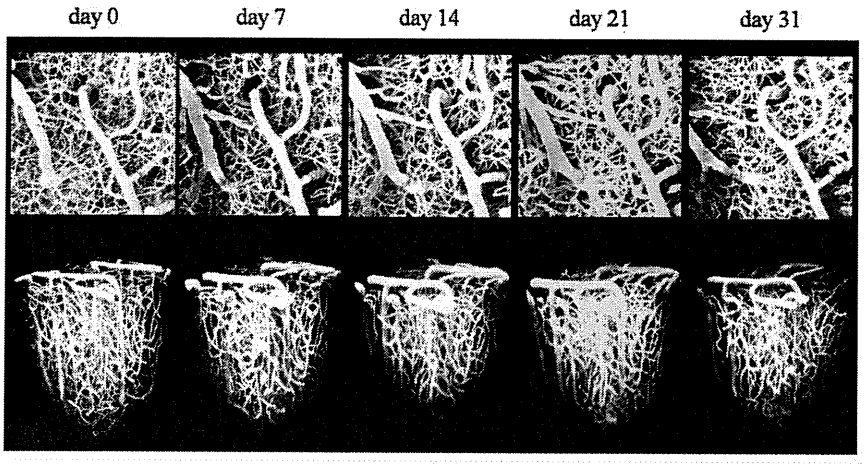

Figure 2. The 3D imaging of cortical microvasculature with two-photon microscopy. Volume images ($0.46\times0.46\times0.80$ mm^3) were obtained from day 0 (start of exposure to 10% oxygen) to day 31 for the identical region within the cortex. The upper panels show the maximum intensity projected images in the x-y plane (0.46×0.46 mm^2), and the lower panels show the 3D reconstructed images.

Journal of Cerebral Blood Flow & Metabolism (2012) 32, 456–467
© 2012 ISCBFM All rights reserved 0271-678X/12 $32.00
www.jcbfm.com

Early and progressive impairment of spinal blood flow–glucose metabolism coupling in motor neuron degeneration of ALS model mice

Kazunori Miyazaki[1], Kazuto Masamoto[2,3], Nobutoshi Morimoto[1], Tomoko Kurata[1], Takahumi Mimoto[1], Takayuki Obata[2], Iwao Kanno[2] and Koji Abe[1]

[1]*Department of Neurology, Okayama University Graduate School of Medicine, Dentistry and Pharmaceutical Science, Okayama, Japan;* [2]*Department of Biophysics, Molecular Imaging Center, National Institute of Radiological Sciences, Chiba, Japan;* [3]*Education and Research Center for Frontier Science and Engineering, University of Electro-Communications, Tokyo, Japan*

The exact mechanism of selective motor neuron death in amyotrophic lateral sclerosis (ALS) remains still unclear. In the present study, we performed *in vivo* capillary imaging, directly measured spinal blood flow (SBF) and glucose metabolism, and analyzed whether if a possible flow–metabolism coupling is disturbed in motor neuron degeneration of ALS model mice. *In vivo* capillary imaging showed progressive decrease of capillary diameter, capillary density, and red blood cell speed during the disease course. Spinal blood flow was progressively decreased in the anterior gray matter (GM) from presymptomatic stage to 0.80-fold of wild-type (WT) mice, 0.61 at early-symptomatic, and 0.49 at end stage of the disease. Local spinal glucose utilization (LSGU) was transiently increased to 1.19-fold in anterior GM at presymptomatic stage, which in turn progressively decreased to 0.84 and 0.60 at early-symptomatic and end stage of the disease. The LSGU/SBF ratio representing flow–metabolism uncoupling (FMU) preceded the sequential pathological changes in the spinal cord of ALS mice and was preferentially found in the affected region of ALS. The present study suggests that this early and progressive FMU could profoundly involve in the whole disease process as a vascular factor of ALS pathology, and could also be a potential target for therapeutic intervention of ALS.
Journal of Cerebral Blood Flow & Metabolism (2012) **32,** 456–467; doi:10.1038/jcbfm.2011.155; published online 9 November 2011

Keywords: ALS; flow–metabolism uncoupling (FMU); G93A; local spinal glucose utilization (LSGU); spinal blood flow (SBF)

Introduction

Amyotrophic lateral sclerosis (ALS) is a progressive and fatal disease that is caused by the selective death of motor neurons. Approximately 5% to 10% of patients have a genetically inherited form known as familial ALS. About 15% to 20% of familial ALS cases are associated with missense mutations or small deletions in the gene that encodes Cu/Zn-superoxide dismutase 1 (SOD1) (Aoki *et al*, 1993; Rosen *et al*, 1993). Transgenic (Tg) mice that carry mutant SOD1 genes have been generated to elucidate how mutations in the SOD1 gene cause motor neuron death (Gurney *et al*, 1994; Murakami *et al*, 2007). Although the underlying mechanism of ALS has not yet been fully clarified, several reports have demonstrated noncell autonomous death of motor neurons (Boillee *et al*, 2006; Clement *et al*, 2003; Llinas *et al*, 2004; Nagai *et al*, 2007; Pramatarova *et al*, 2001; Wang *et al*, 2005).

During physiological conditions, there was a close relationship between blood flow and glucose metabolism (flow–metabolism coupling; FMC) (Leybaert, 2005; Weir *et al*, 2002), and this coupling was tightly controlled through functional regulation of neurovascular unit (NVU) (del Zoppo, 2010). Structural and functional abnormalities in this NVU have not been fully elucidated under pathological conditions (Lo and Rosenberg, 2009) especially in ALS. Several reports have demonstrated the reductions of blood

Correspondence: Professor K Abe, Department of Neurology, Okayama University Graduate School of Medicine and Dentistry, 2-5-1 Shikata-cho, Okayama 700-8558, Japan.
E-mail: gmd20021@s.okayama-u.ac.jp
This work was partly supported by Grant-in-Aid for Scientific Research (B) 21390267 and the Ministry of Education, Science, Culture and Sports of Japan, and by Grants-in-Aid from the Research Committee of CNS Degenerative Diseases (Nakano I), and grants (Nishizawa M, Mizusawa H) from the Ministry of Health, Labour and Welfare of Japan.
Received 5 June 2011; revised 9 September 2011; accepted 26 September 2011; published online 9 November 2011

flow and glucose metabolism in the cerebral cortex and the spinal cord of both ALS patients and the animal model (Dupuis *et al*, 2011; Guo *et al*, 2000; Waldemar *et al*, 1992; Zhong *et al*, 2008). Furthermore, we have very recently found that the damage in NVU was observed before motor neuron degeneration (Miyazaki *et al*, 2011), which may be an important pathologic pathway in human and animal model of ALS.

It remains still unclear whether if a possible FMC abnormality is present in ALS, and if such a FMC abnormality is related to motor neuron degeneration. In the present study, therefore, we performed *in vivo* capillary imaging and directly analyzed the FMC with spinal circulation and glucose metabolism.

Materials and methods

Animal Models

During the experiment, the animals were treated in accordance with the declaration of Helsinki and the guiding principles in the care and use of animals. Also, all experimental and animal care procedures were approved by the Animal Care and Use Committee of the Graduate School of Medicine, Dentistry, and Pharmaceutical Science of Okayama University. A Tg mouse line with the G93A human *SOD1* mutation (G1H/+) was obtained from Jackson Laboratories (Bar Harbor, ME, USA) and maintained as hemizygotes by mating Tg males with C57BL/6J females. The offspring were genotyped using a PCR assay with DNA obtained from tail tissue samples. We used 12-, 16-, and 19-week-old (W) G93A mice and age-matched non-Tg C57BL/6J littermates (wild type, WT) as controls. The 12-W Tg mice were considered to be at the presymptomatic stage, the 16-W mice to be at the early-symptomatic stage, and the 19-W mice to be at the end stage of the disease.

In Vivo Imaging of Spinal Capillary Vessels

For *in vivo* imaging, 12, 16, and 19 W of Tg mice ($n=5$, 6, 8 at each W), and 19 W of WT littermates ($n=5$) were used. The animals were initially anesthetized with 2% isoflurane and maintained with 1% during surgical procedures. Rectal temperature was maintained at 37.0°C ± 0.2°C by means of a feed back-controlled warm pad. The back of the animal was shaved, and the midline incision of the skin was made to expose the back musculature. The paravertebral muscles were carefully removed from the vertebral column, and laminectomy of the lumber vertebrae at the level of L4–5 was performed. Bleeding was controlled either by coating bone wax or by using small pieces of gelatin sponges (Astellas Pharma, Tokyo, Japan). For visualization of the spinal vasculature, a bolus of Qdot605 (2 μmol/L in 50 μL buffered solution; Invitrogen, Carlsbad, CA, USA) was injected from tail vein. Mice were put in lateral decubitus position, and the spinal column was stabilized by placing two of the spinal clamps along the anterior–posterior axis using stabilized devise as described in previous report (Davalos *et al*, 2008) with some modifications. A small well of Gelseal (GE HealthCare, Milwaukee, WI, USA) was built around the exposed spinal cord and filled with physiological saline, followed by immersion of ×20 objective lens (0.5 Na; Leica Microsystems, Wetzlar, Germany). The spinal vasculature was visualized with multiphoton excitation fluorescent microscope (TSC SP5; Leica Microsystems) at 900-nm excitation (Mai Tai HP; Spectra-Physics, Santa Clara, CA, USA) with an emission band-pass filter of 655/50 nm. Images were captured toward anterior horn (AH) region up to 500 μm depth from the spinal surface with a step size of 0.01 mm in the *z*-direction. A single capillary was defined as the single vessel having crosssectional thickness <8 μm and for both edges continued to two new vessels as a branching, and the capillary diameter was measured using LAS AF software (Leica Microsystems). Capillary density was measured as percentage of area using ImageJ software (National Institutes of Health, Bethesda, MD, USA). For creation of Figures 1A–1D, each image was converted to TIFF format using LAS AF software and three continuous images were merged using photoshop software (Adobe, San Jose, CA, USA). The red blood cell (RBC) velocity was measured by tracking RBC that appeared as dark segment against brilliant plasma background through single capillary. Time-lapse images were obtained by line scan in each single flame, and image processing and calculation of average RBC velocity in each capillary were performed as described (Autio *et al*, 2011).

Histological Pathology

For histological pathology, 12, 16, and 19 W Tg mice ($n=5$ at each W), and 19 W WT littermates ($n=5$) were used. Each mouse was deeply anesthetized and transcardially perfused with heparinized saline, followed by 4% paraformaldehyde in 0.1 M phosphate buffer (pH 7.4). The lumbar spinal cord spanning L4–5 was removed and further fixed by immersion in the same fixative for 4 hours and then frozen after cryoprotection with a series of phosphate-buffered sucrose solutions of increasing concentration (10%, 15%, and 20%). Transverse sections of 12 μm thickness were cut through the lumbar cord with a cryostat following cresyl violet staining (Nissl stain).

Measurement of Spinal Blood Flow

For the measurement of spinal blood flow (SBF), 12, 16, and 19 W of Tg mice ($n=6$, 5, 5 at each W), and age-matched WT littermates ($n=5$ at each W) were used. Prior to experiment, HR (heart rate) and blood pressure (SBP (systolic blood pressure), MBP (mean blood pressure), and DBP (diastolic blood pressure)) were measured by tail-cuff method in each mouse (PB-98A; Softron, Tokyo, Japan). Spinal blood flow was determined by the standard autoradiographic ^{14}C-iodoantipyrine (IAP) method as described (Sakurada *et al*, 1978) modified for mice (Jay *et al*, 1988). Briefly, the animals were initially anesthetized with 2% isoflurane and maintained with 1% in 69% N_2O/30% O_2, and polyethylene catheters (Neuroscience,

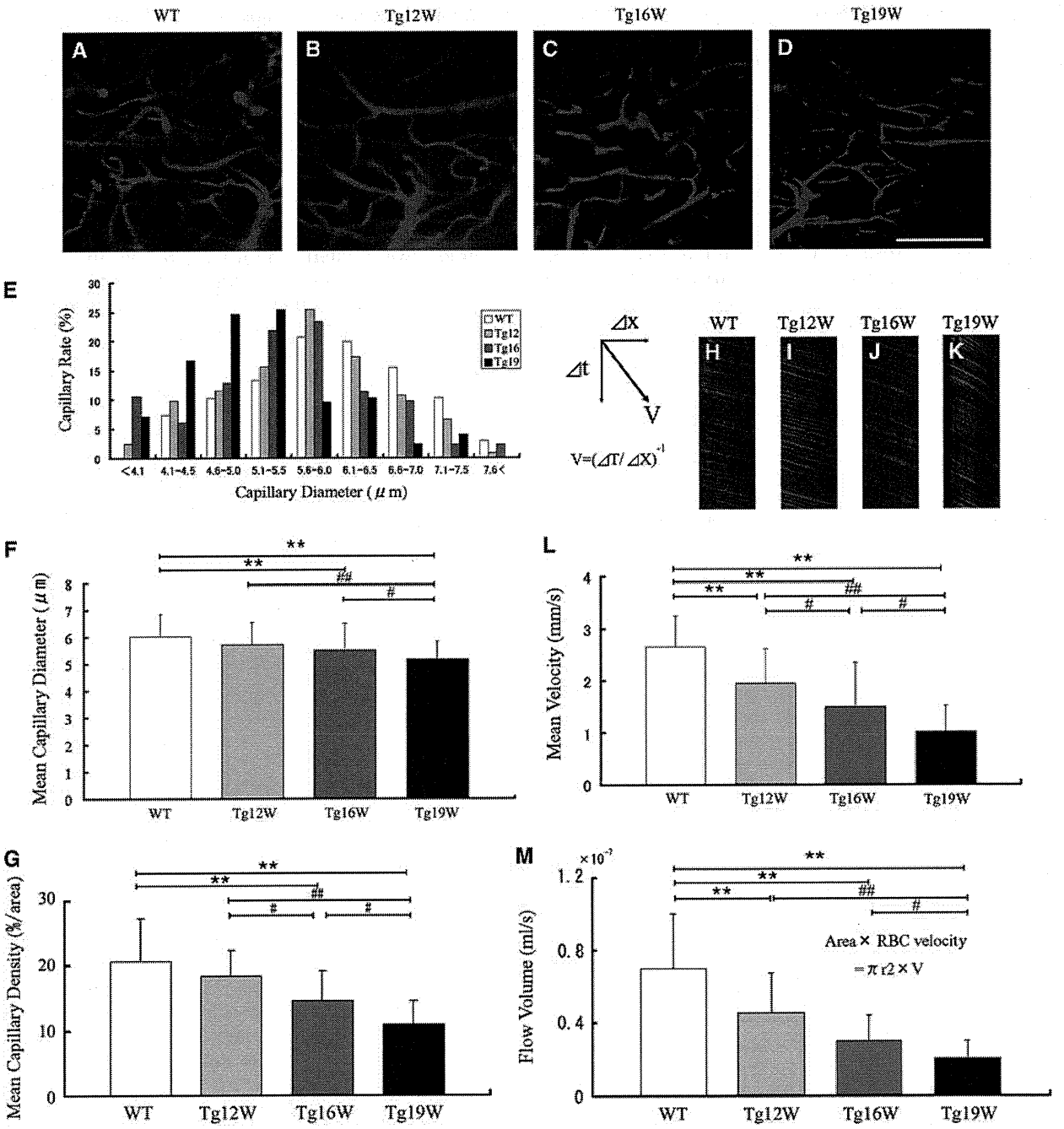

Figure 1 *In vivo* capillary vessel imaging in the anterior horn (AH) of lumbar cord in wild-type (WT; 19 W; **A**) and G93A-transgenic (Tg) mice at 12, 16, and 19 W (**B–D**). Scale bar = 100 μm. Frequency distribution histograms of the number of capillaries (percent in total counted capillaries) according to diameter (**E**), mean capillary diameter (**F**), and mean capillary density (**G**) during the disease course. Line scans of microvessels in the lumbar AH (**H–K**). Red blood cells (RBCs) appeared as dark segment against brilliant plasma background through single capillary. Mean RBC velocity (**L**). Flow volume calculated from RBC velocity and diameter in each capillary (**M**). $^{**}P < 0.01$ versus WT mice. $^{\#}P < 0.05$, $^{\#\#}P < 0.01$ versus Tg mice in different W.

Tokyo, Japan) were inserted into the left femoral artery and vein. Arterial blood was collected, and physiological parameters such as Hct (hematocrit), Hb (hemoglobin), pH, PO_2, PCO_2, and HCO_3 were measured (iSTAT300F, Fuso Pharmaceutical Industries, Osaka, Japan). ^{14}C-IAP (5 μCi in 100 μL of physiological saline; Perkin-Elmer Life and Analytical Sciences, Boston, MA, USA) was injected continuously via the femoral venous catheter. During injection, timed arterial blood was collected in preweighed tubes, and volume was calculated. Blood samples were resolved in tissue solubilizer (Perkin-Elmer), reacted with hydrogen peroxide to reduce quenching, added 3 mL of

scintillation fluid (Clear-Sol II, Nacalai tesque, Kyoto, Japan), and ^{14}C-IAP concentration was determined using liquid scintilation counter (TRICARB; Packard Instrument, Downers Grove, IL, USA). Precisely 1 minute after the IAP injection, mice were decapitated. The spinal cords were rapidly removed, frozen on a powdered dry ice, cut into 20 μm sections on a cryostat, and dried on a hot plate at 55°C. The sections were subject to autoradiography with ^{14}C-standards on an imaging plate (BAS-SR, Fujifilm, Tokyo, Japan) for 7 days, and autoradiograms were captured by image reader (FLA-7000, Fujifilm). Local tissue ^{14}C-concentrations were determined according to standards using densitometric analysis software (Multi Gauge Ver3.0, Fujifilm). The regions of interest were placed on five regions in gray matter (GM) (right and left AH, middle region of AH, right and left dorsal horn (DH)), and four regions in white matter (WM) (anterior funiculus, right and left lateral funiculus, and dorsal funiculus). Local SBF was calculated from the tissue concentration of ^{14}C-IAP and timed tracer concentration in the arterial blood according to the operational equation as described (Sakurada *et al*, 1978). Mean SBF for each region was determined by three contiguous sections in each regions of interest.

Measurement of Local Spinal Glucose Utilization

With a different set of mice group, 12, 16, and 19 W of Tg mice ($n=6$, 5, 5 at each W, and age-matched WT ($n=5$ at each W), were used for the measurement of local spinal glucose utilization (LSGU). Local spinal glucose utilization was determined by the standard autoradiographic ^{14}C-2-deoxyglucose (DG) method as described (Sokoloff, 1977). Briefly, the animals were inserted catheter under isoflurane condition. ^{14}C-2DG (3 μCi in 50 μL of physiological saline; Perkin-Elmer) was intravenously injected, and timed arterial blood was collected. The blood samples were centrifuged, and plasma glucose (Glucose analyzer, Pilot) and tracer ^{14}C-concentrations (Liquid Scintillaqtion Counter, Packard Instrument) were determined. After 45 minutes experimental period, spinal cords were removed, sectioned, and autoradiography was performed as described above. The setting of regions of interest and densitometric methodology were as same as SBF measurement described as above. Local spinal glucose utility was calculated from the tissue concentration of ^{14}C-2DG, timed tracer concentration and glucose concentration in the arterial plasma according to the operational equation with a lumped constant for rat as described (Sokoloff, 1977). Mean LSGU for each region was determined by three contiguous sections in each regions of interest.

Statistical Analysis

For the *in vivo* imaging analysis, differences among the each group were evaluated with one-way analysis of variance with normal distribution followed by the Tukey–Kramer test. Statistical differences in the physiological parameters, SBF, and LSGU analyses between the age-matched WT and Tg mice were evaluated by Student's *t*-test with normal distribution. A probability value <0.05 was regarded as statistically significant. Parametric data were presented as mean ± s.d.

Results

Physiological Parameters

There was no significant difference in physiological parameters (HR, SBP, MBP, DBP, Hct, Hb, pH, PO_2, PCO_2, and HCO_3) in Tg mice compared with age-matched WT mice (Table 1).

In Vivo Imaging of Spinal Capillary Vessels

There were considerable amount of blood vessel capillaries in the lumbar spinal GM of the WT with a diameter <8 μm (Figure 1A), but less dense in the (WM) (data not shown). The diameter of capillary vessels apparently became smaller in Tg mice with disease progression, and density of the capillary vessels progressively became lower (Figures 1B–1D).

Table 1 Physiological parameter

	12 W		*16 W*		*19 W*	
	WT (n = 5)	*Tg (n = 6)*	*WT (n = 5)*	*Tg (n = 5)*	*WT (n = 5)*	*Tg (n = 5)*
HR (b.p.m.)	679 ± 12	664 ± 15	682 ± 33	688 ± 40	692 ± 32	665 ± 85
SBP (mm Hg)	104 ± 3	110 ± 3	118 ± 10	112 ± 9	112 ± 8	112 ± 5
MBP (mm Hg)	81 ± 2	82 ± 2	85 ± 6	80 ± 7	81 ± 6	84 ± 4
DBP (mm Hg)	70 ± 1	68 ± 2	69 ± 7	64 ± 7	65 ± 7	71 ± 6
Hct (%)	38.4 ± 5.5	39.1 ± 7.8	37.6 ± 6.9	39.2 ± 6.1	40.2 ± 5.0	39.0 ± 6.2
Hb (g/dL)	13.2 ± 1.9	13.2 ± 2.5	13.0 ± 1.3	11.3 ± 4.8	13.7 ± 1.7	13.5 ± 1.9
pH	7.32 ± 0.07	7.34 ± 0.08	7.33 ± 0.06	7.33 ± 0.08	7.33 ± 0.06	7.29 ± 0.06
PO_2 (mm Hg)	123 ± 17	141 ± 20	114 ± 18	110 ± 28	106 ± 29	131 ± 33
PCO_2 (mm Hg)	38 ± 6	40 ± 7	32 ± 9	41 ± 5	35 ± 10	42 ± 7
HCO_3 (mmol/L)	20.8 ± 2.8	22.0 ± 2.3	20.6 ± 2.0	22.7 ± 3.6	20.9 ± 3.3	22.5 ± 4.0

DBP, diastolic blood pressure; Hb, hemoglobin; Hct, hematocrit; HR, heart rate; MBP, mean blood pressure; SBP, systolic blood pressure; Tg, transgenic; WT, wild type.

The histograms of capillary diameter gradually shifted from the right (large) to the left (small) with age in Tg mice (Figure 1E, gray to black bars), with the average of capillary diameter of progressive smaller among WT, Tg12, Tg16, and Tg19 W of $6.01 \pm 0.84\,\mu m$, $5.72 \pm 0.81\,\mu m$, $5.50 \pm 0.99\,\mu m$ ($^{**}P<0.01$ versus WT), and $5.16 \pm 0.68\,\mu m$ ($^{**}P<0.01$ versus WT, $^{\#\#}P<0.01$ versus Tg12, $^{\#}P<0.05$ versus Tg16) (Figure 1F). Mean capillary density measured as percentage of area showed progressive decrease from 20.7% in WT mice to 18.3% in Tg12 W, 14.6% in Tg16 W ($^{**}P<0.01$ versus WT, $^{\#}P<0.05$ versus Tg12), and 10.8% in Tg19 W ($^{**}P<0.01$ versus WT, $^{\#\#}P<0.01$ versus Tg12, and $^{\#}P<0.05$ versus Tg16) (Figure 1G). The mean RBC speed in a single capillary significantly decreased with disease progression (Figures 1H–1L), from 2.66 ± 0.59 mm/s of WT to 1.95 ± 0.65 mm/s of Tg12 W ($^{**}P<0.01$ versus WT), 1.50 ± 0.85 mm/s of Tg16 W ($^{**}P<0.01$ versus WT, $^{\#}P<0.05$ versus Tg12), and 1.01 ± 0.51 mm/s of Tg19 W ($^{**}P<0.01$ versus WT, $^{\#\#}P<0.01$ versus Tg12, and $^{\#}P<0.05$ versus Tg16), respectively. Flow volume was calculated from RBC velocity and diameter in each capillary, and showed significant decrease with disease progression in $0.70 \pm 0.30\ 10^{-7}$ mL/s in WT, $0.46 \pm 0.21\ 10^{-7}$ mL/s in Tg12 W ($^{**}P<0.01$ versus WT), $0.30 \pm 0.14 \times 10^{-7}$ mL/s in Tg16 W ($^{**}P<0.01$ versus WT), and $0.20 \pm 0.10\ 10^{-7}$ mL/s in Tg19 W ($^{**}P<0.01$ versus WT, $^{\#\#}P<0.01$ versus Tg12, and $^{\#}P<0.05$ versus Tg16), respectively (Figure 1M).

Histological Analysis

Nissl staining of the lumbar cord revealed that there were a number of large motor neurons in the AH of WT mice (Figure 2A). Although the number of motor neuron of Tg mice was similar to that of WT mice at 12 W (Figure 2B), it decreased progressively to ~78% of WT level at 16 W ($^{*}P<0.05$), and 35% at 19 W ($^{**}P<0.01$) (Figures 2C and 2D).

Spinal Blood Flow

In WT mice, SBF of GM was much higher than that of WM, and was slightly increased with normal aging from 12 to 19 W (Table 2; Figures 2E, 2I, 2M, and 3A–3I). Anterior horn showed a trend toward higher SBF than DH in cervical, thoracic, and lumbar regions (Table 2). As compared with age-matched WT mice, significant reduction of SBF was found in GM of Tg mice as early as 12 W, especially AH of cervical (−20%, $^{**}P<0.01$ in AH; −15%, $^{**}P<0.01$ in DH), thoracic (−16%, $^{*}P<0.05$ in AH), and lumbar cord (−24%, $^{**}P<0.01$ in AH; −18%, $^{**}P<0.01$ in DH), except for dorsal region of thoracic cord (Table 2; Figures 2F, 2J, 2N, 3A, 3D, and 3G). In contrast, there were no significant changes of SBF in any region of WM at 12 W. At 16 W of Tg mice, the reduction of SBF was progressively exacerbated in GM, and the reduction rate of SBF was prominent in AH (−39%, −32%, and −45% in cervical, thoracic, and lumbar cord, respectively, $^{**}P<0.01$ in each), and not so prominent in DH (−23%, −20%, and −32% in cervical, thoracic, and lumbar cord, respectively, $^{**}P<0.01$ in each), resulting in dissociative reduction of SBF between AH and DH (Table 2; Figures 2G, 2K, 2O, 3B, 3E, and 3H). There was no significant difference of SBF in WM too at this 16 W. At 19 W of Tg mice, the reduction of SBF in GM was further aggravated in cervical (−52%, $^{**}P<0.01$ in AH; −48%, $^{**}P<0.01$ in DH), thoracic (−41%, $^{**}P<0.01$ in AH; −35%, $^{**}P<0.01$ in DH), and lumbar cord (−56%, $^{**}P<0.01$ in AH; −50%, $^{**}P<0.01$ in DH) (Table 2; Figures 2H, 2L, 2P, 3C, 3F, and 3I). At this 19 W, SBF was only slightly reduced in WM especially lateral funiculus of cervical (−22%, $^{**}P<0.01$) and lumbar cord (−23%, $^{**}P<0.01$).

Local Spinal Glucose Utility

In WT mice, there were higher levels of LSGU in GM than WM of cervical, thoracic, and lumbar cords (Table 3; Figure 2Q, 2U, 2Y, 3J–R). The LSGU of AH had higher tendency than that of DH in each part of spinal cord, and LSGU were slightly decreased with normal aging from 12 to 19 W (Table 3). Transgenic mice at 12 W showed significant increases of LSGU in GMs of cervical (+8%, $^{*}P<0.05$ in AH) and lumbar cord (+18%, $^{**}P<0.01$ in AH; +16%, $^{*}P<0.05$ in DH) (Table 3; Figures 2R, 2V, 2Z, 3J, 3M, and 3P). No significant difference of LSGU was observed in GM of thoracic cord, or WM of all spinal cord regions at 12 W. In Tg mice at 16 W, significant reductions of LSGU were observed in GM regions of cervical (−23%, $^{**}P<0.01$ in AH; −35%, $^{**}P<0.01$ in DH) and lumbar spinal cord (−28%, $^{**}P<0.01$ in AH; −33%, $^{**}P<0.01$ in DH) (Table 3; Figures 2S, 2W, 2AA, 3T, 3W, and 3Z). There was no significant change in GM of thoracic cord and WM of all levels of spinal cord. In Tg mice at 19 W, the LSGU further decreased in GMs of cervical (−42%, $^{**}P<0.01$ in AH; −45%, $^{**}P<0.01$ in DH), thoracic cord (−45%, $^{**}P<0.01$ in AH; −45%, $^{**}P<0.01$ in DH), and lumbar cord (−40%, $^{**}P<0.01$ in AH; −35%, $^{**}P<0.01$ in DH) (Table 3; Figure 2T, 2X, 2AB, 3L, 3O, and 3R). Local spinal glucose utilization were slightly reduced in funiculus at this 19 W in cervical (−35%, $^{**}P<0.01$ in lateral funiculus; −21%, $^{*}P<0.05$ in dorsal funiculus), thoracic (−29%, $^{*}P<0.05$ in anterior funiculus; −30%, $^{**}P<0.01$ in lateral funiculus), and lumbar cord (−35%, $^{**}P<0.05$ in lateral funiculus).

Ratio of Local Spinal Glucose Utilization to Spinal Blood Flow

In WT mice, LSGU/SBF ratio of WM was slightly higher than that of GM, which slightly decreased

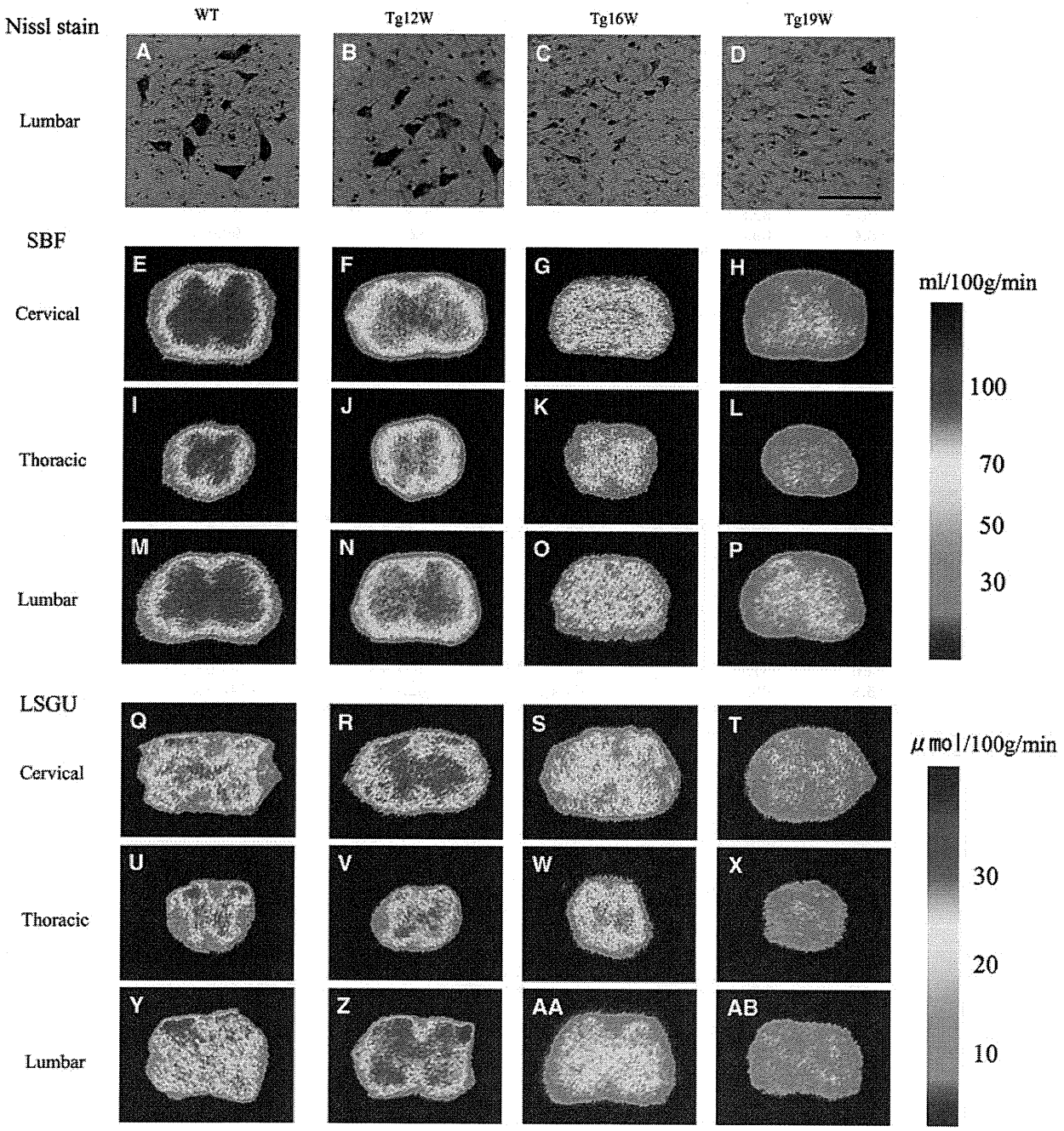

Figure 2 Nissl staining in anterior horn (AH) of lumbar cord in wild-type (WT) and transgenic (Tg) mice (**A–D**). Scale bar = 100 μm. Autoradiograms of spinal blood flow (SBF) in the cervical, thoracic, and lumber cord of WT and G93A-Tg mice (**E–P**). Autoradiograms of local spinal glucose utilization (LSGU) in the cervical, thoracic, and lumber cord of WT and Tg mice (**Q–AB**).

with normal aging from 12 to 19 W. Although the LSGU/SBF ratio remained at about 0.30 in most GM and WM of each spinal level, GM of lumbar cord showed the lowest ratio (0.27 ± 0.02, 0.23 ± 0.02, 0.21 ± 0.01 at 12, 16, and 19 W, respectively) among spinal coronal areas and longitudinal levels. The LSGU/SBF ratio of Tg mice at 12 W were significantly increased in GM of 0.40 ± 0.01 (+29%, $^{**}P<0.01$) in cervical, 0.41 ± 0.02 (+23%, $^{**}P<0.01$) in thoracic, and 0.39 ± 0.04 (+48%, $^{**}P<0.01$) in lumbar cord (Figures 3S, 3V, and 3Y). At 16 W, significant increases of the ratio were also seen in the GM of 0.36 ± 0.01 (+19%, $^{**}P<0.01$) in thoracic and 0.27 ± 0.02 (+15%, $^{*}P<0.05$) in lumbar cord. This increase continued until 19 W in lumbar GM of 0.28 ± 0.02 (+34%, $^{**}P<0.05$), but not seen in cervical and thoracic levels (Figure 3AA). In contrast, there was no significant difference of the LSGU/SBF ratio in WM between WT and Tg mice and no significant change with age in WT and Tg mice at any region (Figures 3S–3AA).